Turbulent mass transfer near gas-liquid interfaces in water and shear-thinning dilute polymer solution

Tom Lacassagne, Mahmoud El Hajem, Jean-Yves Champagne, Serge Simoëns

Turbulent mass transfer near gas-liquid interfaces in water and shear-thinning dilute polymer solution

Tom Lacassagne[a,b,*], Mahmoud EL Hajem[a], Jean-Yves Champagne[a], Serge Simoëns[a,**]

[a] *Laboratoire de Mécanique des Fluides et d'Acoustique, UMR 5509, Univ. Lyon, INSA Lyon, Ecole Centrale de Lyon, Université Claude Bernard Lyon I, CNRS, F-69621, Villeurbanne, France*

[b] *IMT Nord Europe, Institut Mines-Télécom, Univ. Lille, Centre for Energy and Environment, F-59000 Lille, France*

Abstract

Turbulence is known to enhance gas-liquid mass transfer and mixing of high Schmidt number dissolved gases in water by deforming the concentration boundary layer that develops at the interface. Fundamental mechanisms of surface renewal and injection have been progressively evidenced throughout the last decades, *via* fundamental experiments of low mean shear turbulence interacting with flat interfaces in water. However, and despite the obvious influence of non-Newtonian behaviours on gas liquid mass transfer in industrial and environmental applications, not such study exists (to the best of the author's knowledge) on whether and how these mechanisms apply in shear-thinning dilute polymer solutions (DPS). Following a previous work on near surface hydrodynamics, turbulent mass transfer and mixing is studied in a weakly shear-thinning fluid, and compared to the Newtonian, water case. Stereoscopic Particle Image Velocimetry (SPIV) and Inhibited Planar Laser Induced fluorescence are used simultaneously to measure the local liquid phase velocity and dissolved gas concentration fields respectively. Coupled measurements are used to estimate the turbulent mass fluxes, which are interpreted using a conditional quadrant analysis. Results show that in DPS as well as in water, surface renewal is the most frequent mechanism, but injection events are the most efficient in terms of mass transfer. Even

*tom.lacassagne@imt-nord-europe.fr

**serge.simoens@ec-lyon.fr

at a low concentration, the polymer significantly modifies the signature of those mass transfer events, by enhancing scalar stretching and injection mass transfer outside of the viscous sub-layer, altering classical gradient models.

Keywords: Turbulence, mass transfer, shear-thinning, PIV, PLIF, quadrant analysis

1. Introduction

Turbulence is known to be a highly efficient enhancement mechanism for mixing and mass transfer between phases. In particular, liquid side turbulence has been shown to enhance air-water mass transfer of low diffusive atmospheric gases at interfaces, by locally deforming the liquid side concentration boundary layer [1, 2, 3]. Local, near-surface, mixing mechanisms occur in thin sub-layers under the interface, typically of 1 cm to less than 1 mm. They have been investigated for several decades, but the question of their depiction is arduous to tackle, both numerically and experimentally, because of the small scales involved. Studies have so far focused mostly on air-water interfaces, clean [4, 5, 6, 7, 8] or polluted [9, 10]. Despite the numerous industrial processes involving turbulent gas-liquid mass transfer in complex fluids (see e.g. [11],[12]) local mass transfer events and near-surface turbulence have never been measured in non-Newtonian media. Here, focus is made on the case of a low liquid phase diffusivity atmospheric gas, carbon dioxide, frequently encountered in industrial and environmental applications. Indeed, capture and storage of carbon dioxide is a crucial challenge for industrial and environmental process aiming at an increased sustainability [13, 14, 15], and many of such process involve flows of liquids with complex rheologies [15, 16].

The aim of this work is to provide a first experimental observation of near-surface turbulence-induced mass transfer and mixing in a non-Newtonian, moderately shear-thinning fluid, in the few millimetres underneath a flat gas-liquid interface. The gas is dissolving from an over saturated gaseous phase at rest towards a complex liquid phase, at initially zero concentration, stirred by bulk turbulence. The simplified case of a flat horizontal interface is studied in order to visualize fundamental mass transfer mechanisms at small scales. Spatially and temporally synchronised application of stereoscopic particle image velocimetry (SPIV) and planar laser induced fluorescence (PLIF) allows to measure coupled liquid phase velocity fluctuations and dissolved gas

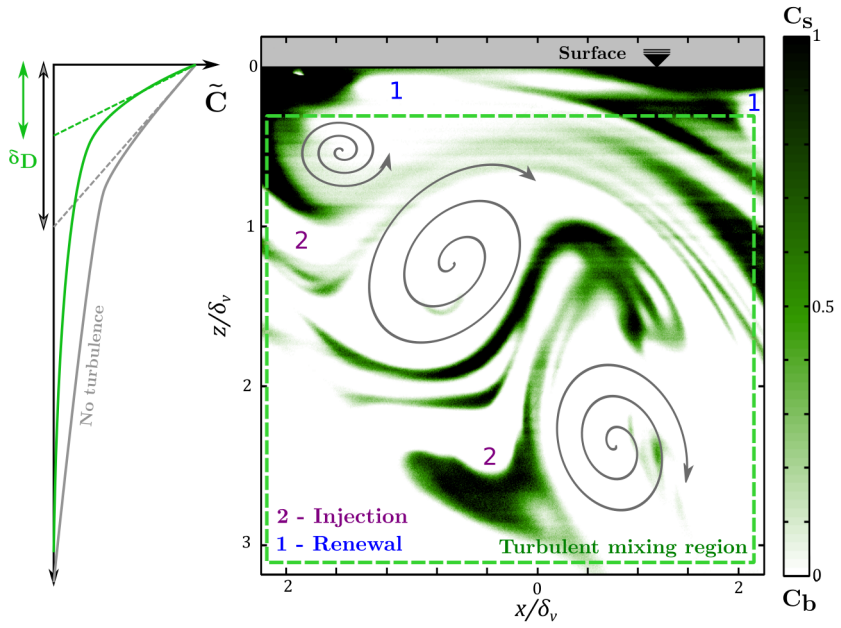

Figure 1: Principles of turbulent mass transfer at a flat interface. Left: contraction effect of the apparent diffusive boundary layer in presence of turbulence. Right: illustration of surface renewal and peeling/injection events and of the typical scalar sub-layers, from PLIF measurements presented hereinafter.

concentration fluctuations, and thus access local turbulent mass fluxes. Conditional quadrant analysis of mass fluxes leads to the accurate observation and description of mass transfer mechanisms near the gas-liquid interface, and how they are affected by the shear-thinning rheology. First order gradient modelling is developed in order to obtain values of eddy diffusivity and characteristic time coefficients.

2. Background

In a liquid phase in contact with an over-saturated gas phase, the concentration C of a dissolved species varies exponentially between its interfacial value C_{sat} and the bulk value C_b far from the interface, according to Fick's laws of diffusion. One may write

$$\tilde{C}(z,t) = \frac{C(z,t) - C_b(t)}{C_{sat}(t) - C_b(t)} = e^{-z/\delta_D} \tag{1}$$

where $\tilde{C}(z,t)$ is the concentration normalised by saturation and bulk concentrations, t is the time and z the distance from the interface (here the depth below the flat horizontal interface, see fig 1).

Assuming a negligible resistance to mass transfer on the gas side, the saturation value is fixed by the partial pressure of the same species in the gaseous phase p^* according to Henry's law $p^* = H_{c,i}C_{sat}$[17]. Resistance to mass transfer on the liquid side is expressed by the δ_D parameter: the apparent diffusive layer depth, or liquid film. This sub-layer accounts for diffusion but also advection mechanisms. In cases with no liquid side motion, this sub-layer is simply equivalent to a purely diffusive sub-layer. The liquid side mass transfer efficiency/velocity is defined $k_L = \frac{D}{\delta_D}$ is with D the molecular diffusion coefficient of the dissolved gas in the aqueous medium considered [18], with here $D = 1.90 \times 10^{-9}$ m^2.s^{-1} for carbon dioxide in water at 20°C. The relative effects of momentum diffusion over molecular diffusion are quantified by the Schmidt number Sc$= \nu/D$ with ν the kinematic viscosity of the fluid.

For high Schmidt number (low diffusivity) phenomena, flow structures may deform, contract or stretch the local diffusive layer δ_D. What is known of turbulence action on dissolved gas at the interface can thus be summarized as follows (see figure 1). A turbulent eddy coming from the bulk enters the surface influenced region and is deformed by surface action [4, 5, 19]. If its typical size is large compared to the apparent scalar sub-layer depth, it mainly contracts the scalar sub-layer thus sharpening the concentration gradient and increasing mass transfer. This is the picture of the film model by [18]. Smaller eddies however have the ability to peel the diffusive film and send saturated fluid downwards, while replacing it with fresh fluid brought from the bulk. Under-saturated fluid being brought at the interface, concentration gradients are increased making the boundary layer δ_D thinner and enhancing near surface diffusion. This is the principle of surface renewal or film renewal [20, 21, 6]. This renewal is associated with a complementary mechanism [22, 1, 23, 2]: injection/peeling events of the boundary layer by velocity structures resulting in the injection of saturated fluid inside the bulk where i) diffusion is thus enhanced and ii) multi-scale turbulent mixing becomes dominant. The wide range of turbulent structure sizes and the various ways eddies can interact with the scalar boundary layer result in an intricate combination of surface renewal and injection events responsible of global turbulent mass transfer.

The influence of turbulence on gas-liquid mass transfer and the depths at

which it is relevant thus needs to be understood in light of the behaviour of turbulence approaching the interface. In water, the interactions between an horizontal free surface and upcoming bulk turbulence are usually characterized using two "undisturbed" scales of turbulence [24, 5]: the horizontal integral length scale L_∞ and horizontal velocity fluctuations (root mean square value) u'. These are the values that would be found at the interface location if there were no interface, obtained by extrapolation of the bulk turbulence scaling laws [25]. They thus depend on the bulk turbulence properties only. The depth at which turbulence begins to "see" the interface is called the surface-influenced layer, and is assumed to be about the size of one integral length scale of the upcoming bulk turbulence L_∞ [4, 5, 6]. Velocity dynamics in the surface-influenced layer is mostly independent of the surface boundary condition, and the theory of [4] applies equally well to clean, contaminated and no-slip surfaces up to a certain proximity with the interface [26], which is in turn defined by another smaller typical depth: the viscous sub-layer δ_v, scaling as $\delta_v = L_\infty Re_T^{-0.5}$ [5, 27]. Here Re_T is the turbulent Reynolds number at the interface expressed as $Re_T = \frac{\rho u' L_\infty}{\mu}$, with ρ and μ the density and dynamic viscosity respectively. This sub-layer is defined as the depth from which an eddy adjusts to the boundary condition set by the interface by viscous effects. For turbulent mass transfer of high Schmidt number gases at non negligible Reynolds number, the characteristic scalar depth δ_{OD} is typically smaller than the viscous sub-layer depth δ_v: most of the events relevant for mass transfer occurs within the viscous sub-layer.

In a recent work [19], the liquid phase velocity data of the present set of measurements presented has been used to extend this description to the case of shear-thinning dilute polymer solutions (DPS). A correlation for the evolution of the viscous sub-layer depth in the dilute regime of shear-thinning inelastic xanthan gum (XG) solutions has been derived. The increase of the viscous sub-layer depth was smaller than what could be expected from the increase in zero shear rate viscosity, and better correlated to the value of the infinite-shear viscosity. In what follows, comparison is made between a Newtonian case and a shear-thinning case with comparable Reynolds number and viscous sub-layer depth. In that way, scalar and mass transfer events can be compared between the Newtonian and shear-thinning case for equivalent hydrodynamic conditions of up-coming turbulence.

It should also be mentioned that the influence of non-Newtonian properties on turbulent or non-turbulent mass transfer can be found addressed

from a global, process oriented point of view in the literature, where studies try to relate the evolution of global mass transfer parameters such as the volumetric mass transfer coefficient k_La, to dimensionless numbers describing the non-Newtonian properties of the flow. This has been done on a large variety of two phase flows, among which aerated stirred tanks [28, 29, 30, 11] and bubble columns [31, 12, 32], to cite a few. The fundamental limitation in these configurations is that mass transfer depends on both the mass transfer velocity k_L but also on the interfacial area a, both of which are modified by non-Newtonian properties: hydrodynamics of the liquid phase act on the gas phase properties, that is to say the bubble size, size dispersion, rising velocity, or residence time [28, 32] making it difficult to disentangle the two effects and isolate from such studies the effects of turbulence and non-Newtonian fluids on mass transfer velocity and mixing alone. This is why fundamental, local, flat surface experiments are essential first steps to the better understanding of non-Newtonian turbulent mass transfer.

3. Materials and methods

3.1. Shear-thinning polymer solutions

Distilled water and a dilute solution of XG (10 ppm concentration, $M_w = 3.4 \times 10^6$ g.mol^{-1}, polydispersity close to 1.12 [33]) are used as the Newtonian and shear-thinning fluid, respectively. XG yields clear aqueous non-Newtonian solutions suitable for the use of optical methods metrology, and is here chosen for its high resistance to strong shears and extreme pH conditions [34]. Such features are necessary when using it in the oscillating grid apparatus, in which strong local shear may be experienced by polymer chains nearby the grid, and when dissolving carbon dioxide in the liquid phase, a process during which the pH may decrease to acidic values. The polymer concentration is chosen well inside the dilute regime [35, 25]. It is assumed that the diffusion coefficient of carbon dioxide in the aqueous medium is not modified by the presence of the polymer chains in this dilute concentration limit [36]. The weak shear-thinning behaviour of such a solution is measure on an Anton-Paar MC302 rheometer and modelled by a Carreau-Yasuda equation $\frac{\mu-\mu_\infty}{\mu_0-\mu_\infty} = \left(1 + \left(t_{CY}\dot{\gamma}\right)^m\right)^{\frac{n-1}{m}}$ with $\mu_0 = 1.30$ mPa.s the zero shear rate viscosity, $\mu_\infty = 0.99$ mPa.s the infinite shear rate Newtonian plateau, $t_{CY} = 0.08$ s the characteristic time scale of the polymer, n-1=-0.4 the shear-thinning power law exponent, and m =2 the transition parameter. Viscoelasticity is checked to be negligible at this concentration

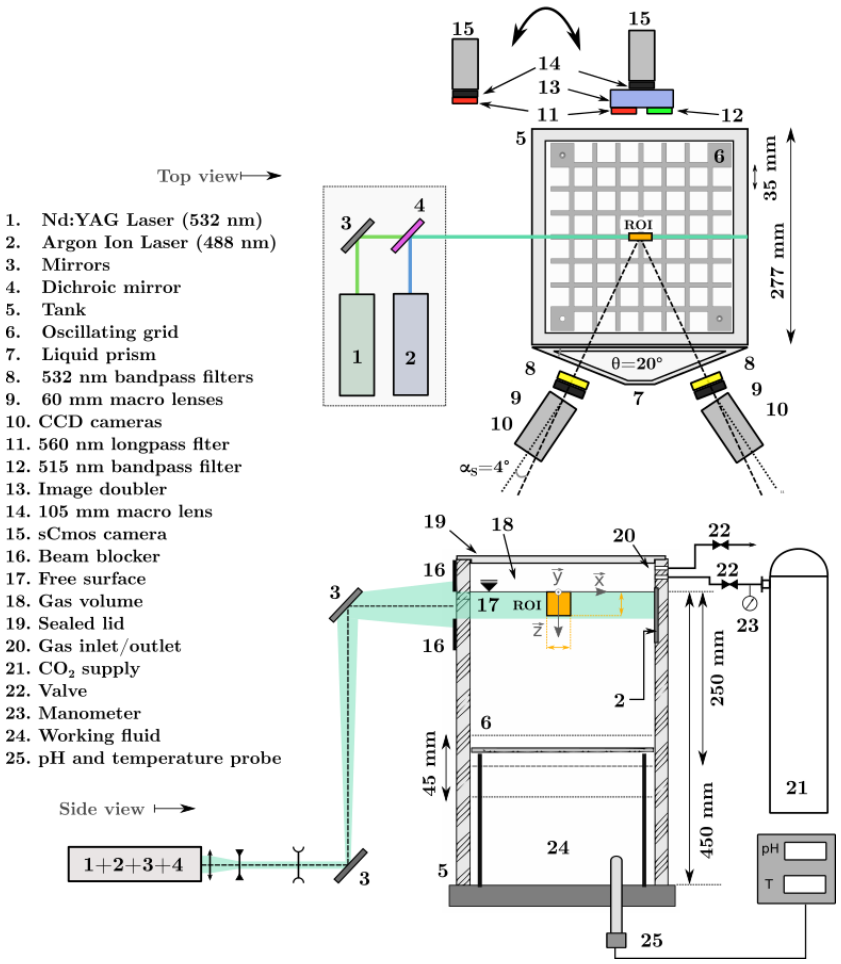

Figure 2: Sketch of the experiment set-up for coupled measurements.

[35, 25]). Moreover, in the context of the near surface turbulence results [19], this low concentration allows for comparable viscous sub-layer depth and turbulence properties within the viscous sub-layer between water and XG solution, and hence the mass transfer events are compared in equivalent hydrodynamic conditions. Here the viscous sub-layer depth is 5.10 mm for water and 5.64 mm for the DPS case (see table 1).

3.2. Turbulence generation

Turbulence is generated in the liquid phase by an oscillating grid device previously described and used in [25, 37, 19, 38, 39], and sketched in figure 2.

The transparent tank has a 277 mm by 277 mm inner cross section, the fluid height is set at H=450 mm and the distance between the surface and the average grid position is 250 mm. The grid oscillations frequency is f =1 Hz and the Stroke (amplitude) is 45 mm. A Cartesian squared-meshed grid is used, the grid mesh size (distance between the center of two successive grid bars or holes) being 35 mm (see figure 2). With the very dilute solution considered here, the mean flow structure and mean flow to turbulence ratio are close to that achieved in water, and the mean flow is considered weak enough not to affect our local mass transfer study [25]. When the grid is oscillated, the flat surface hypothesis is verified up to sub-millimetric vertical oscillations of the surface (about 1.5 % of the viscous sub-layer depth) caused by the in and out motion of the grid supporting rods [19]. Special care is taken to ensure that both the water and DPS experiments are performed in clean interface conditions (see [19]). The undisturbed velocity and length scales are estimated from [25, 19] and reported in table 1. The table also shows the corresponding values of the interface Reynolds number based on the maximum viscosity, $Re_T = \frac{\rho u' L_\infty}{\mu_0}$. Note that Re_T slightly decreases in the polymer case, mostly because it is defined on μ_0, which may not be a representative viscosity of the flow [19]. The Deborah numbers based on the shear-thinning time scale t_{CY} and on the grid oscillations period is $De = t_{CY} f = 0.08$.

3.3. Concentration and velocity measurements

3.3.1. Methods

Dissolved CO_2 concentration fields are measured using fluorescein-based inhibited fluorescence techniques: $I_{pH} - PLIF$ [40]. For the DPS case, a ratiometric improvement of the method, $I^r_{pH} - PLIF$, described in [41], was also applied. This ratiometric method also allows to reduce noise and systematic error of $I_{pH} - PLIF$ on quantitative measurements at high concentration values, very close to the interface (see [42], appendix G). The spatial scales and the shape of concentration structures are by no mean dependent on the method used. Hence for the purpose of the present work where only a qualitative and conditional analysis of the concentration field is required, the two methods are equivalent. Hereinafter and if not specified differently, all water and DPS results presented come from respectively $I_{pH} - PLIF$ and $I^r_{pH} - PLIF$ measurements. In each case, fluorescein sodium concentration in the working fluid is $C_{Fl} = 5 \times 10^{-7}$ mol.L^{-1}. Fluorescence is triggered by a Stabilite 2017 Argon-Ion Continuous Wave Laser (CWL). The

Parameter	Water	DPS
μ (mPa s)	1.0	1.0-1.3
L_∞ (mm)	24.5	45.6
δ_v (mm)	5.10	5.64
Re_T	110	106-110
Sc	527	527-686
De	0	0.08
δ_D (mm)	0.50	0.20
$\delta_D^e = 2L_\infty Re_T^{-1/2} Sc^{-1/2}$ (mm)	0.25	0.34-0.38
$\delta_B^e = 2L_\infty Re_T^{-3/4} Sc^{-1/2}$ (mm)	0.063	0.11-0.12

Table 1: Hydrodynamic parameters and mass transfer sub-layers of the two working fluids. L_∞ and δ_v were determined in [19], by interpolation of bulk turbulence scaling [25] or directly measured, respectively. The expected apparent diffusive sub-layer δ_D^e and Batchelor sub-layer δ_B^e are computed as $\delta_D^e = 2L_\infty Re_T^{-1/2} Sc^{-1/2}$ and $\delta_B^e = 2L_\infty Re_T^{-3/4} Sc^{-1/2}$ respectively [22]. The experimental apparent diffusive layer δ_D is derived from measured concentration profiles (figure 3). For the DPS, Re_T, Sc, δ_D^e and δ_B^e are viscosity dependent: ranges based on maximum and minimum viscosity values are reported.

effective maximum output power is 0.6 W and the laser sheet thickness is $e_{Ar} = 250$ μm. Fluoresced light intensity fields are recorded by a Lavision sCMOS camera (2560 by 2160 pixel sensor) equipped with a 105 mm focal length Macro lens. For $I_{pH} - PLIF$ measurements, the lens is only equipped with a long-pass filter to suppress the PIV and fluorescence excitation wavelengths from measured intensities. For $I^r_{pH} - PLIF$ measurements, an image doubler is added in front of the lens. One "eye" of the doubler is equipped with a 515 nm bandpass filter, and the other with a 560 nm cut-off long-pass filter. The camera is used in its single frame configuration with an opening time of $\mathrm{dt}_f = 10$ ms, and an acquisition frequency of $f_{acq} = 4$ Hz (bounded by that of SPIV, [19]). Calibration procedures described in [40] and [41] are respectively applied when using intensity (I) based $I_{pH} - PLIF$ or ratio (R) based $I^r_{pH} - PLIF$. They both consist in recording sets of fluorescence images at different homogeneous pHs in the region of interest (ROI), and building either pixel by pixel I=f(pH) or unique R=f(pH) calibration curves (available in appendix Appendix A), where I is the total fluoresced light intensity and R the intensity ratio of two fluoresced light spectral bands (two colours). Dissolved gas concentration versus pH equilibria in water are solved

numerically using Matlab (see [42]). For the small amount of polymer added, it is checked experimentally that the addition of XG does not modify these equilibria. The relationship between pH and dissolved gas concentration is $C = Ae^{-BpH}$ with A=1.55×10^{11} mg/L and $B = 4.63$. Using a method described in [41], the relative uncertainty on the ratio in for $I^r_{pH} - PLIF$ is estimated to be below 1.2%. The maximum relative uncertainty on pH is close to 1%, relative uncertainties on concentration are below 10% for pH<5 and pH>6.5. As for the 1 color PLIF technique, relative uncertainties still fall below 5% in the same range, however additional errors due to reflection and darker stripes are introduced, which can multiply the uncertainty by a factor of 10.

Liquid phase velocity measurements in the vicinity of the interface are achieved by SPIV and have already been reported in [19], where all the experimental details can be found. The experimental set-up is sketched in figure 2. In this study, the velocity fields are revisited and analysed in combination with concentration fields. Spatial calibration of all cameras is performed by taking separate images of a LaVision standard reference pattern, and simultaneous images of a transparent test pattern placed inside the fluid prior to the experiment. Concentration and velocity fields are coupled using a binning procedure: the spatial resolution of the scalar field is reduced to that of the vector field by spatially averaging the concentration value in each SPIV interrogation window projected on the scalar field. In other words, SPIV sets the resolution limit the mass transfer study. Note that this "full average binning" [41] is sightly different from the "binning at center" method used by [2]: "full average" binning tends to reduce the noise associated to concentration measurement by smoothing over a wider span than "binning at center", and is more consistent in terms of processing with SPIV, which is also window-based.

3.3.2. Experimental protocol and definition of concentration statistics and convergence

The tank is first filled with the working fluid and fluorescein sodium is added. Dissolved carbon dioxide concentration is increased up to its gas saturation limit and the first PLIF calibration image (lower pH) is recorded. This concentration is then gradually decreased by nitrogen stripping, and calibration images are recorded for decreasing dissolved gas concentrations (higher pH) until the fluid is cleared from any dissolved carbon dioxide. The corresponding initial pH and dissolved gas concentration are measured, as the

initial condition of the experiment. Grid oscillations are started, followed by PIV and PLIF recording once the oscillating grid turbulence is established and stationary, and the volume of gas above the interface is instantly replaced by pure carbon dioxide (injection time <10 s). Rheological measurements are performed on the DPS before and after the experiments to check that no polymer degradation occurs.

Concentration fields are inherently transient: at a given point in the flow, concentration varies with time due to both diffusion acting on $\overline{C}$ and turbulence causing c', where $\overline{C}$ denotes the mean concentration field (statistical average) and c' the turbulent fluctuations. Statistical analysis of concentration fields would in principle require performing many trial in similar conditions, which is impracticable given the time and resource cost of each mass transfer experiment. The estimation of mean and fluctuating concentrations from such transient measurements is thus rather done as in [2]. The instantaneous concentration fields are first averaged over the horizontal dimension x (operator $[.]_x$) into the quantity $[C(z,t)]_x$ (see figure 3). The expected concentration values $C_E(z,t)$ are then obtained by exponential fitting time series of $[C(z,t)]_x$ at all z with expressions of type $C_E(z,t) = k_c(z)(1 - e^{-k_{t1}(z)t - k_{t2}(z)t^2})$. $C_E(z,t)$ estimates the concentration that would be expected without the presence of turbulent scalar structures. It is assumed in the following that $C_E(z,t) \equiv \left[\overline{C}\right]_x(z,t)$, or in other words that the expected concentration is equivalent to a statistical average. Concentration fluctuations are subsequently defined as $c'(x,z,t) = C(x,z,t) - \left[\overline{C}\right]_x(z,t)$. With this definition, there is no need to demonstrate the statistical convergence of the mean concentration. The computation of second order statistical properties such as root-mean-square (rms) of concentration fluctuations (or, later, turbulent mass fluxes) is made on time intervals of 1050 s (between $t = 200$ s and $t = 1250$ s for water and between $t = 700$ s and $t = 1750$ s for DPS, see figure 3 c,d). The typical lifetime of a scalar event can be estimated from the integral time scale (see section 4.1.4). Here the order of magnitude of integral time scale of concentration fluctuations is 10 s and so the time intervals used are at least 100 times greater than the typical scalar eddy turnover, which is deemed sufficient for statistical convergence.

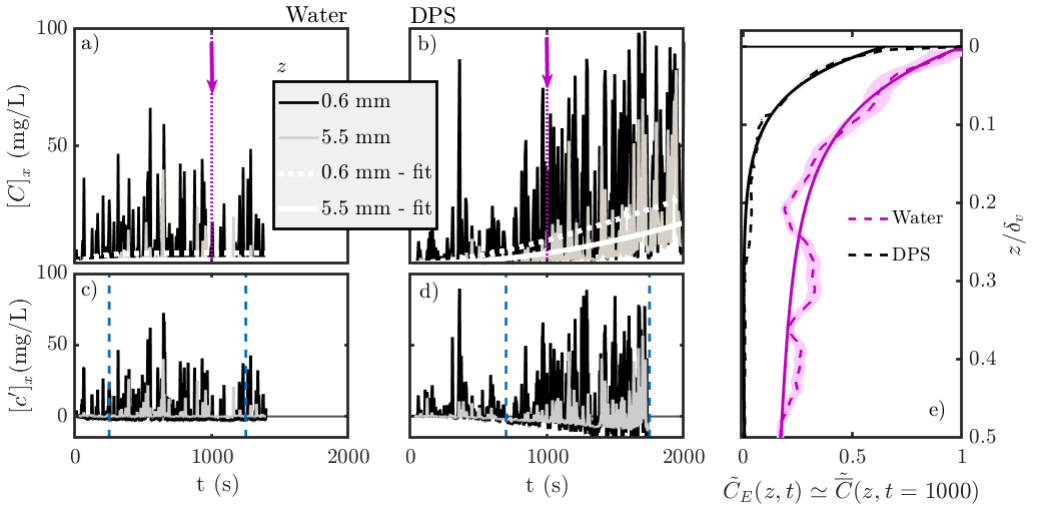

Figure 3: Time series of mean concentration (a,b) and of concentration fluctuations (c,d) for water (a,c) and DPS (b,c) respectively, at two different depths. e) Average concentration profiles at t=1000 s, dotted lines representing measured data and full lines the expected concentration fittings C_E.

4. Results and discussion

4.1. Scalar properties

4.1.1. Scalar structures

An example of instantaneous concentration field (in water) is shown in figure 1. The colors scale is for $(C - C_b)/(C_s - C_b)$ with C_b and C_s the bulk and interfacial values, of order 10^{-2} mg/L and 10^0 mg/L respectively (note that $C_s \leq C_{sat}$ as discussed below). Concentration is higher close to z/δ_v=0 (location of the gas liquid interface) and decreases with increasing z. Between the interface and the bulk, a complex combination of high concentration structures exists: these are characteristic of injection events. One also notices that the concentration near the interface can locally and instantaneously be close to C_b, when highly concentrated fluid at the interface is replaced by fresh one coming from the bulk as part of the renewal mechanism. Measurements in the purely diffusive case (no fluid motion) were not conducted in the present study. Indeed, when dissolved in a fluid at rest (in equivalent vertical configurations) dissolved carbon dioxide is known to trigger gravitational instabilities [43], which quickly disrupt the diffusive boundary layer, and would have made such measurements unsuitable for com-

parison. It is worth mentioning that the theoretical saturation concentration predicted by Henry's law is here never measured in the ROI. Typical concentrations at the smallest measurable depths ($z \simeq 200$ μm) only reach up to 100 mg/L (fluctuating both in time and space for water and DPS), about 10 times lower than the 1394 mg/L value given by Henry's law. It is likely that Henry's law saturated CO_2 concentration value were also not measured in sub-surface measurements of [2] and bubble-wake measurements of [40] (both using $I_{pH} - PLIF$) or in the works of [22, 1] on sub-surface oxygen dissolution. This difference between the maximum measured concentration and the theoretical C_{sat} may be ascribed to the limited sensitivity PLIF techniques i) in the high concentration range (concentrations higher than about 100 mg/L, corresponding to pH lower than 4.5 that cannot be measured efficiently since fluorescence intensity levels at pH 4 and 4.5 are similar) and ii) the possibility for surface renewal and injection events to sweep concentration patches away from the interface before they have time to reach saturation concentration.

4.1.2. Concentration boundary layer

Example of near-surface (z$< 0.5\delta_v$) expected non-dimensional concentration profiles $\tilde{C}_E(z,t)$ (see section 3.3.2) at t=1000 s are shown in figure 3 e), and fitted by an exponential function similar to equation 1) where C_{sat} is replaced by the apparent interfacial concentration $C_s(t)$. Shaded areas are $\pm 10\%$ uncertainty regions. From this sub-figure it appears that the apparent scalar boundary layer thickness δ_D is close to 0.5$\pm$0.1 mm (z/δ_v=0.098) for the water case, 0.25$\pm$0.02 mm (z/δ_v=0.036) for DPS (table 1) (uncertainties estimated from standard deviation over the statistically stationary range). Measured values are consistent with the range predicted by scaling laws [22] reported in table 1. However, relying on such "Newtonian" scaling, one would have expected δ_D to be larger in the DPS case. This is a first evidence that the non-Newtonian aspect of the fluid, even moderate, makes the DPS behaviour's depart from the expected viscous Newtonian one.

4.1.3. Spatial scalar scales

Now investigating the spatial properties of turbulent scalar structures, the correlation coefficient of concentration fluctuations between two points separated by a distance r_i along spatial dimension i ($i = x, y$ or z), at a given depth z, is defined as $R_c^i(z, r_i) = \left[\frac{\overline{c'(r_i^0,z,t)c'(r_i^0+r_i,z,t)}}{\overline{c'^2}}\right]_x$. An example of correlation coefficients R_c^z plotted versus the separation length r_z along

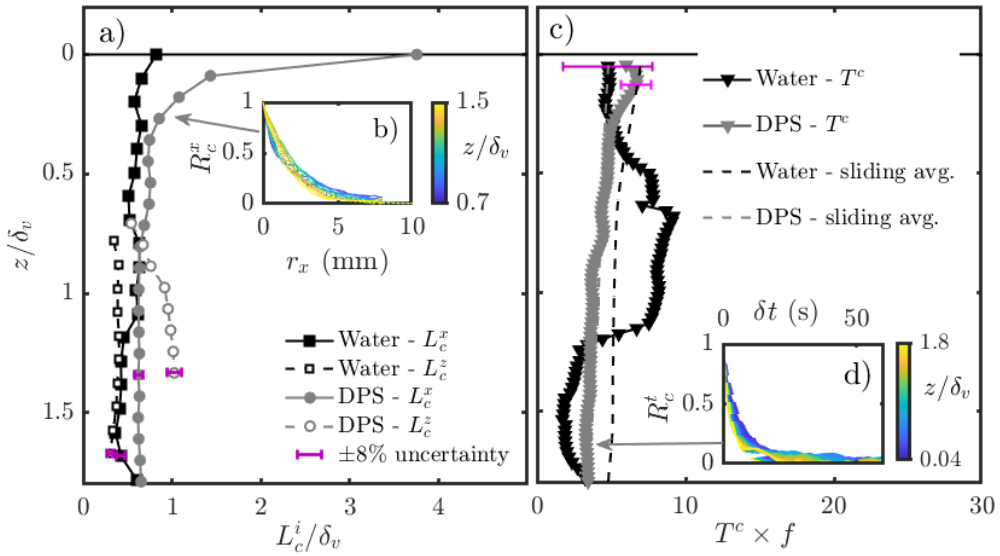

Figure 4: Spatial and temporal concentration integral scales, estimated from the integration of two-points and two-times correlation coefficients of concentration fluctuations, respectively. Spatial: integral length scales for water and DPS (a) and example of corresponding two point concentration correlation coefficient for DPS (b). Full markers are scales along the horizontal dimension, empty markers are scales along the vertical dimension. Full lines in the sub-figure are computed correlation coefficients, dashed lines are exponential fittings. Temporal: integral time scale for water and DPS (c) and example of the corresponding two times correlation coefficient for DPS (d). Time is made non dimensional multiplying by the oscillating grid frequency. Markers in c) are computed scales, dashed lines are sliding average of the computed scales over a 2 mm span ($\simeq 40\%$ of δ_v).

dimension z, for the DPS run, at different depths is shown in the insert of figure 4 b). Correlation curves are fitted by a sum of exponential functions and the spatial integral length scale for concentration along dimension z (vertical scale) obtained by integrating from r_z=0 mm to infinity. A similar process is applied to correlation coefficient along the horizontal direction x. Integral concentration length scale are plotted versus depth in figure 4 a) for both fluids. Vertical length scales are not computed at the smallest depth ($z/\delta_v < 0.7$) due to the size of the sampling region. The 5% confidence interval on exponential fittings is used to estimate a typical uncertainty of $\pm 8\%$ on length scales, illustrated by an error bar on one marker per curve (for readability).

Horizontal length scales L_c^x for water show scattering due to the single color LIF method employed. Nevertheless, it appears to be always greater than the vertical one, L_c^z. The latter stays approximately constant between $z/\delta_v = 0.8$ and $z/\delta_v = 1.4$ at a value around L_c^z/δ_v =0.40. In the same depth range, but also up to $z/\delta_v = 0.20$ the horizontal scale is $L_c^x/\delta_v \simeq 0.5$. For $z/\delta_v < 0.2$, L_c^x/δ_v increases up to its apparent maximum value of 0.84 at $z/\delta_v = 0$. These trends imply that patches of turbulent concentration fluctuations are statistically larger in the horizontal dimension than in the vertical one in water at such depths. The increase of L_c^x near the interface is an evidence of the development of the scalar boundary layer, of depth δ_D under the interface. In this sub-layer, concentration patches appear in this two-dimensional view as large horizontal stripes of high concentration, partially and randomly broken by renewal events (see figure 1). At larger depths, concentration structures are stretched and deformed in an isotropic fashion by turbulence and the length scales in both dimensions tend to similar values with increasing depths, still with a preferential horizontal dimension inherited from the peeling process.

Similarities with water can be found for the integral length scales of the DPS: almost constant horizontal scale in most of the ROI, with an abrupt increase at small z, here for $z/\delta_v < 0.2$. In [19], an increase in the horizontal length scale of horizontal velocity fluctuations was observed in the near-interface region for 100 ppm DPS, consistent with the behaviour observed here. The depth at which L_c^x begins to increase is close to the outer-diffusive sub-layer depth δ_{OD} estimated from the mean concentration profiles. Both vertical and horizontal length scales are always higher in DPS than in water. The value of L_c^x/δ_v at the interface is 3.75, 5 times bigger than the one for water. A striking difference is yet that the vertical length scale is higher than the horizontal one at depths higher than $z/\delta_v = 0.80$. While it stayed quite constant with depth in water, it is here decreasing with decreasing z. DPS thus generally tends to increase the size of concentration patches in all dimensions: DPS has an increased viscosity compared to water, hence increased Kolmogorov and Batchelor scales. However, horizontal scalar patches that can be found in the boundary layer are statistically more horizontally elongated in DPS than in water: they are less likely to be broken by renewal events. Renewal rather takes the form of a contraction of the scalar boundary layer with partial replacement of the saturated fluid from the bottom of the boundary layer. Strong sweeping events locally replacing saturated fluid up to z=0, and leading to a split of the boundary layer are seemingly less

frequent in DPS than in water. Outside of the scalar boundary layer, the presence of polymer promotes vertical elongation of concentration structures. This behaviour is consistent with the modification, upon polymer addition, of near-surface hydrodynamics: vertical elongation of turbulent eddies [19, 42], and modification of inter-component energy transfers, with an enhancement of down-going vertical momentum fluxes, as depicted in [42].

4.1.4. Temporal scalar scales

The temporal concentration correlation coefficient is defined for a given location (x, z) as the correlation between concentration fluctuations at instants t and $t + \delta t$, with δt a small time increment. The correlation coefficient at a given depth z is then $R_c^t(z, \delta t) = \left[\frac{\overline{c'(x,z,t)c'(x,z,t+\delta t)}}{\overline{c'^2}}\right]_x$ as defined by [1]. An example of correlation coefficients R_c^t plotted versus the separation time *deltat*, for DPS, at different depths is shown in the insert of figure 4 d) (the blue curve being the closest to the interface and the yellow curve the furthest). Time correlation curves are non Gaussian and can be fitted by a sum of exponential functions, the numerical integration of which from zero to infinity yields an integral concentration time scale T_c (inasmuch as R_c^t curves fall to zero within the time of measurement). The higher the integral time scale the longer the time available for diffusion. Error bars on T_c profiles in figure 4 c) are estimated as the maximum, among all curves, of the difference between numerical integration of R_c^t at a given depth and analytic integration of its exponential fitting. Uncertainties are typically of ± 3 s for water and ± 1 s for the DPS case (purple and pink error bars). They are shown at a single depth for each curve for clarity reasons.

Integral time scales globally increase with decreasing z, which is consistent with the establishment of a scalar boundary layer close to the interface where turbulent stretching of scalar patches is less intense and diffusion has time to occur. The concentration time scales are quite close for water and DPS: about 3.5 s and 4.1 s at $z/\delta_v = 1.50$ and 5.7 s and 6.8 s at $z/\delta_v = 0.20$ respectively. However, profile for water shows significant scattering, possibly due to the single color method noise being amplified by high order statistical analysis, or to poor convergence of the integral time scale. The temporal resolution of scalar fields is indeed quite low: typical persistence times for concentration are of the order of a few seconds, the exponential fitting of correlation curves is thus done with a limited number of points. In order to estimate the uncertainty of integral time scale measurement, the time scale

for a given fluid and a given depth is additionally computed as the numerical integral of the measured R_c^t curve, using a trapezoidal method and this value is compared to the one obtained by integration of the exponential fitting. The maximum differences found are of about 1 s for the DPS measurement, and 3 s for water.

4.2. Velocity / concentration correlations

Coupled measurements of concentration and velocity fields bring an interesting added value to the concentration field by showing some of the flow structures at the origin of the scalar patches' shapes, and allow to compute local mass fluxes [2]. Figure 5 shows examples of coupled instantaneous (a,b) and fluctuating (c,d) fields for water and DPS. While injection events seem obvious from instantaneous fields (e.g in figure 5 b)), fluctuating fields allow to better visualize surface renewal occurring, for example at $z/\delta_v < 0.35$, $x/\delta_v < 0$ on sub-figure d1)). The 3D views bring additional evidence of the out-of-plane motion. With instantaneous information about velocity and concentration fluctuations, it is possible to compute the ensemble average of velocity-concentration correlations $\overline{u_i' c'}$ and the ensemble rms $\langle u_i' c' \rangle_{rms}$, and plot their width averaged profiles along depth $\left[\overline{u_i' c'}\right]_x$ and $[\langle u_i' c' \rangle_{rms}]_x$ (see figure 6). A $\pm 15\%$ uncertainty is expected, derived from the $\pm 10\%$ and $\pm 5\%$ uncertainties on concentration and velocity measurements respectively [41, 19]. Vertical mass fluxes $\overline{u_z' c'}$ are found to be always positive: turbulence tends to enhance mass transfer. Horizontal turbulent mass fluxes are also significant. They contribute to horizontal turbulent mixing of the dissolved gas, and do not tend to zero here given the narrow ROI considered. Horizontal mass fluxes do not appear isotropic in the x and y direction from figure 6 a), especially for the DPS case. Anisotropy increases for decreasing z in water and stays approximately constant with z in DPS. However, 6 b) shows that in terms of rms, horizontal mass fluxes along x and y are equivalent.

4.3. Conditional analysis of turbulent mass fluxes

Further insight on the mass transfer mechanisms is brought by performing conditional analysis of the coupled velocity and mass fluxes [2]. It consists in sorting local flow events according to the sign of their fluctuation, and performing a conditional analysis of turbulent mass or momentum fluxes based on this sorting [44, 45, 46, 2, 47]. A turbulent event is defined using u_z' and c' instantaneous fluctuations. The joint probability density function (PDF or covariance) $P(u_z', c')$ represents the occurring probability of a turbulent

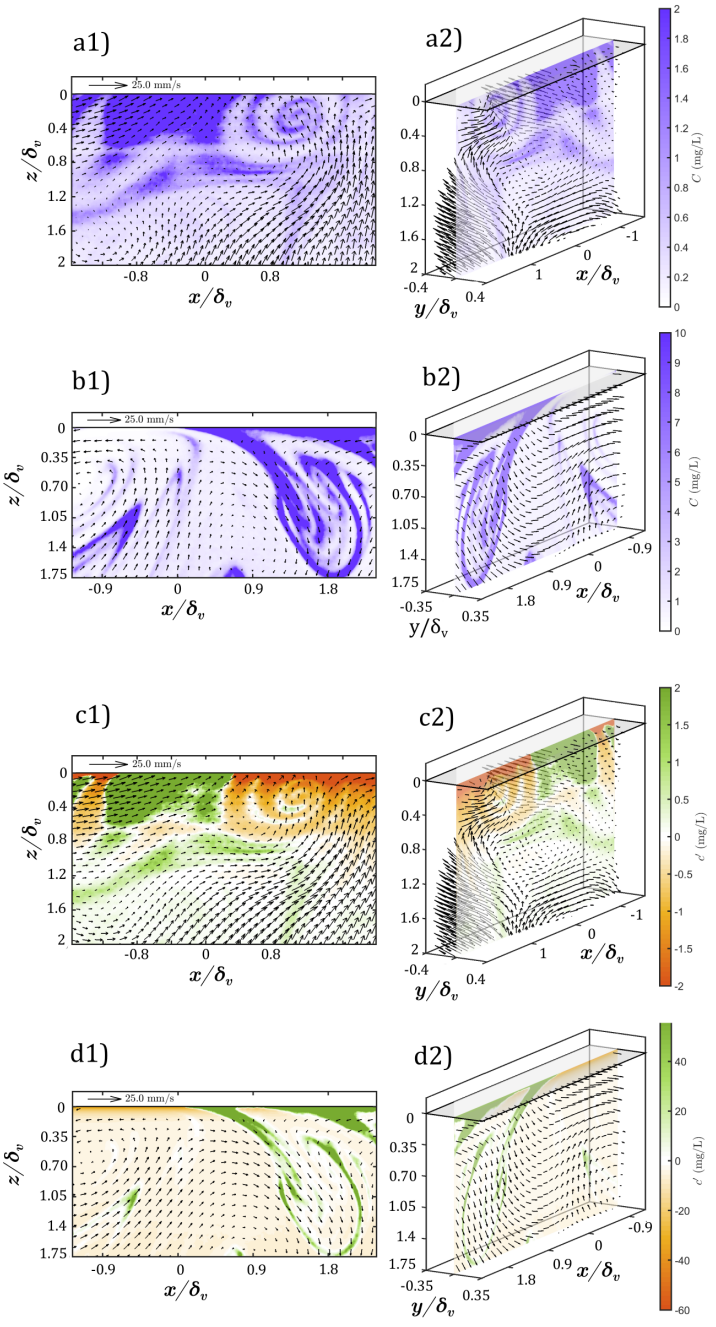

Figure 5: Example of coupled instantaneous (a,b) and fluctuating (c,d) velocity and dissolved gas concentration fields in water (a,c, t=123.5 s) and DPS (b,d, t=1075.25 s). (1) sub-figures are projected 2D views of the (2) plots.

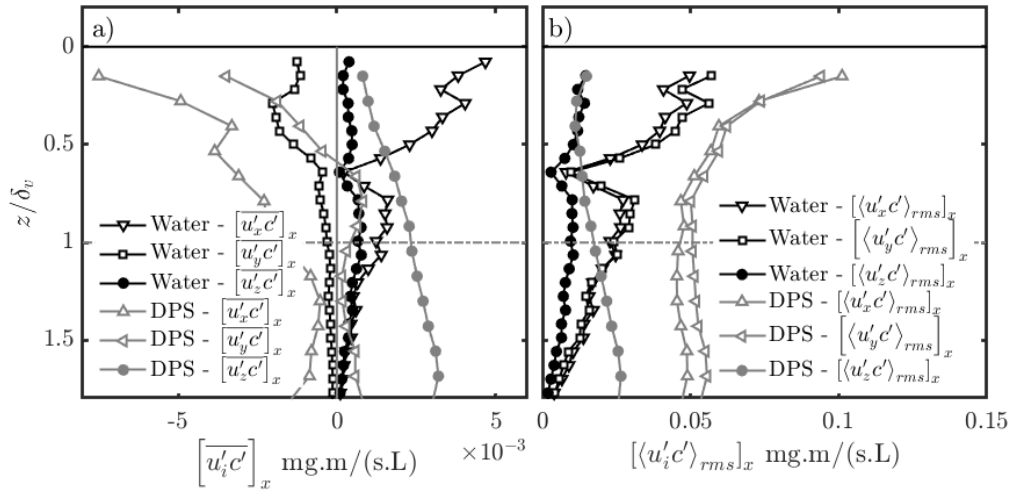

Figure 6: Width averaged profiles of $u'_i c'$ correlations (a) and their rms (b) for water and DPS.

event with fluctuation values equal simultaneously to u'_z and c' at a given location of the flow or in a ROI. The joint PDF is decomposed into four quadrants based on the sign of each fluctuation, according to figure 7. The relative strength of each quadrant can be quantified by the covariance integrand $u'_z c' P(u'_z, c')$. The higher this product the most probable and intense are the event of the associated quadrant. The type of event described by each quadrant is the following:

- **Q1**: Up-going patch of fluid carrying higher dissolved gas concentration. The concentration fluctuation is positive, meaning that the local concentration at the point of interest is higher than the mean concentration at this depth. This higher concentration patch is moved upwards where it merges into an area of higher (equivalent) mean concentration. Q1 events are thus expected to reduce diffusion efficiency.

- **Q2**: Up-going patch of fluid carrying lower dissolved gas concentration. If this low concentration patch enters high mean concentration boundary layer close to the interface, the event can be qualified as a surface renewal event [2].

- **Q3**: Down-going patch of fluid carrying lower dissolved gas concentration. The concentration fluctuation is negative, meaning that the local

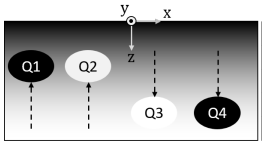

Quadrant	u'_z	c'
Q1	-	+
Q2	-	-
Q3	+	-
Q4	+	+

Figure 7: Principle of quadrant analysis

concentration is lower than mean concentration at this depth. Moving downwards, the scalar patch meets an area of lower dissolved gas concentration. As for Q1 events, Q3 events are expected to reduce diffusion efficiency.

- **Q4**: Down-going patch of fluid carrying higher dissolved gas concentration. The patch of positive concentration fluctuation is moved downwards, towards an area of event lower mean concentration. Diffusion is thus greatly increased. Q4 events correspond to peeling/injection events.

Conditional average of the turbulent mass fluxes can be performed in each quadrant. For example the overall vertical mass flux $\overline{u'_z c'}$ can be decomposed into $\overline{u'_z c'} = \sum \left(P(u'_z, c') \overline{u'_z c'} \right)_{Qi}$ where $\overline{u'_z c'}_{Qi}$ is the contribution of quadrant i to the total flux.

4.3.1. Probability of events

Sub-figures 8 a) show joint PDFs of $\mathrm{P}(u'_z, c')$ for water and DPS in the ranges [-8 8] mm/s for u'_z and [-25 25] mg/L for c'. The same representation is adopted for the covariance integrand in sub-figures 8 b). Close to the surface, a higher probability of negative c' events (Q2,Q3, renewal) is visible. A balancing towards $c' = 0$ with increasing depth is evidenced for water but not so much for DPS. Water PDF figures compare qualitatively well to the results of [2]: a high probability peak at moderate negative c' and a long tail of low probability events at low u'_z and positive c', reducing with depth. Covariance integrand, are also quite similar (keeping in mind that $u'_z > 0$ here corresponds to $u'_z < 0$ in [2]). The major difference with [2] experiments that can be observed in both PDF and covariance integrand plots is that sufficient depths to observe an even balance between quadrants is not attained here. In DPS, a persistence of large amplitude negative c' events with increasing depth is visualized. From the covariance integrand plot of figure 8 b), it

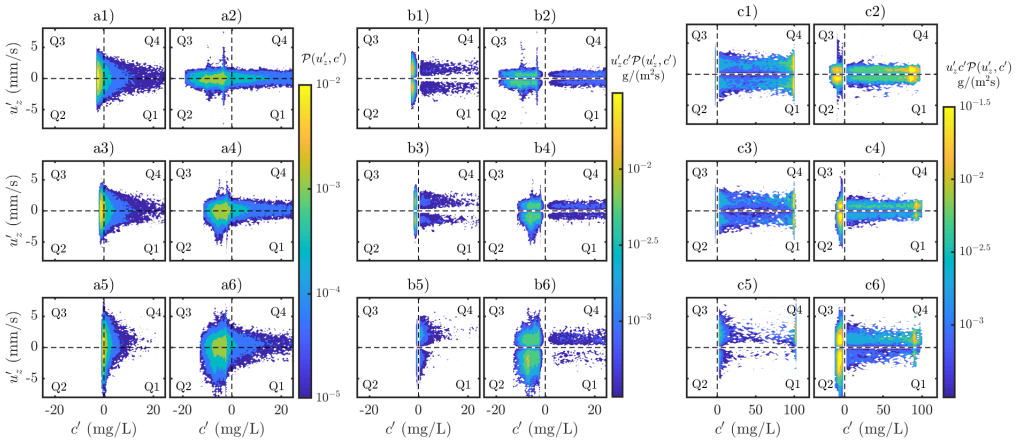

Figure 8: Joint PDF (a) and covariance integrand (b,c) of u_z' and c' for $c' \in$[-25 25] mg/L (a,b) and $c' \in$[-25 125] mg/L (c), for water (abc, odds) and DPS (abc, evens). Results are shown at three sample depths: $z/\delta_v = [0.15, 0.35, 1.10]$ for water, $z/\delta_v = [0.15, 0.41, 0.92]$ for DPS (sub-plots 1 and 2, 3 and 4, 5 and 6 respectively). The variable space is divided in 101 bins in both dimensions. Contour plots of are shown at values regularly distributed along a log scale indicated by the color bars.

appears that injection events are also significant. As in water, the tail of low u_z' and positive c' events reduces with increasing depth.

Covariance integrand plots show that even if the quadrants are quite balanced at larger depths, Q4 events are more probable than Q1 and Q2 than Q3. We thus here evidence the existence of surface renewal (Q2) and injection (Q4) mechanisms in DPS. In order to get access to the high c' injection events, covariance integrand plots are plotted this time expanding to $c' \in$ [-25 125] mg/L (sub-figures 8 c). This new representation confirms what was visible of injection events: the tail at large positive c' values progressively disappears with increasing z for both water [2] and DPS. The existence of two covariance integrand peaks at high positive c', characteristic of strong injection events in the Q4 case is observed.

The peak at c' value close to 100 mg/L is explained by the limitations of the PLIF measurements, which saturates concentration fields at this value due to reduced pH sensitivity at pHs lower than 4. We infer that a similar feature would have been present in the results of [2] if a broader concentration fluctuation range had been considered for result display (as in figure 8 sub-plots c). With a sufficient measurement accuracy at lower pHs, the peak would likely spread over a wider range of high c' values. On this new

representation of the covariance integrand, Q2 and Q3 events completely disappear from the water balance at high depths, for which a combination of high and low c', Q1 and Q4 events dominate. In DPS, Q2 and Q3 events still persist at high depths. The balance between Q1 and Q4 events, which was at equilibrium at small z, is shifted towards Q4 for increasing concentration.

Joint PDF and covariance integrand plots thus bring several information on vertical turbulent concentration events:

- The most probable events are those at moderate negative c', for water and DPS. Positive c' events are displayed over a wider range of c' values.

- At small depths for water and DPS, joint PDF and covariance plots are symmetric with respect to the $u'_z = 0$ axis. With increasing depths, the dominance of Q2 over Q3 and Q4 over Q1 begins to emerge, especially in DPS. Injection (Q4) and renewal (Q2) events are thus confirmed to contribute to mass transfer in both water and DPS.

- From covariance integrand plots, one clearly sees that even if they are less probable than renewal events, injection events are associated to stronger fluctuations.

The probability of each type of events is plotted as a function of depth in figure 9. To do so, the probability of each quadrant type $\mathcal{P}_{Qi}$ is evaluated at each point of the ROI by counting the number of occurrence N_{Qi} of each type of event at this location and dividing by the total number of instantaneous fields N_{tot} such that $\mathcal{P}_{Qi} = \mathrm{N}_{Qi}/\mathrm{N}_{tot}$. $[\mathcal{P}_{Qi}]_x$ is then simply the width-averaged profile of $\mathcal{P}_{Qi}$. Q2 and Q3 probabilities are higher that Q1 and Q4 ones close to the z=0 interface in both water and DPS. This corresponds to the shift of c' PDF's towards negative fluctuations observed in 8 a). In DPS, quadrants with $c' < 0$ are more probable than those associated to $c' > 0$ at all depths, which is another evidence of the preserved dominance of concentration renewal with increasing depth. For water Q1 and Q4 quadrants show higher probability at depths $z/\delta_v > 1.40$. The main difference between water and DPS is found in the evolution of probabilities with depth. In water, the probability of Q2 and Q3 events increases with decreasing z, and the probability of Q1 and Q4 events decreases. For water, the probability of injection (Q4) and renewal (Q2) events are equivalent at moderate depths, leading to symmetrical c' PDFs. When approaching the interface however, the probability of injection events (Q4) decreases versus that of renewal events (Q2),

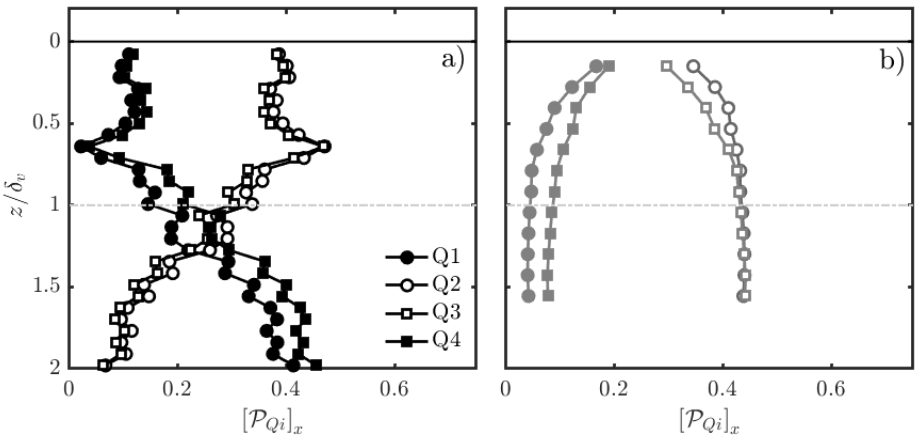

Figure 9: Width averaged probability profile of each quadrant in water (a) and DPS (b). The horizontal line marks the viscous sub-layer depth z=δ_v.

leading to a shift in concentration PDFs towards negative values. In DPS, renewal events (Q2) are always more probable that injection ones. Yet, the probability of these renewal events decreases when approaching the interface, while that of injection events increases. This probability only indicates the likeliness of each type of events to occur, but not the strength of the related mass transfer.

4.3.2. Quadrant analysis of vertical mass fluxes

To tell which events are the most relevant in terms of turbulent mass fluxes, quadrant averaged vertical mass fluxes $\overline{u'_z c'}_{Qi}$ are computed for each point of the ROI, and the absolute value of their width averaged profile are plotted as a function of depth on figure 10 a) and b) for water and DPS. The ±15% uncertainty error bars are shown for only one curve per sub-plot for clarity. For water, Q1 and Q4 quadrant corresponding to positive concentration fluctuations yield higher turbulent mass fluxes than quadrants Q2 and Q3, especially at z< δ_v. Turbulent mass fluxes of all quadrants increase with decreasing z, but Q1 and Q4 increase faster than Q2 and Q3, thus increasing their share in the total turbulent mass flux when approaching the interface. Values of Q1 and Q4 and Q2 and Q3 are respectively close, but at all depths though, $\overline{u'_z c'}_{Q4} > \overline{u'_z c'}_{Q1}$ and $\overline{u'_z c'}_{Q2} \geq \overline{u'_z c'}_{Q3}$, thus confirming that both renewal and injection events tend to create positive turbulent mass fluxes and enhance mass transfer. Injection events are the

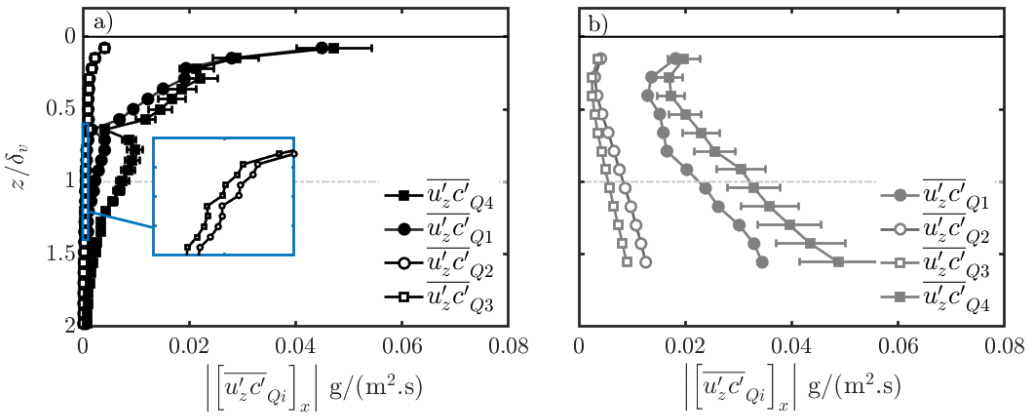

Figure 10: Quadrant sorted vertical turbulent mass fluxes $\overline{u'_z c'}$ as a function of depth, in water (a) and DPS (b). The horizontal dashed-dotted line marks the viscous sub-layer depth z=δ_v. ±15% error bars are shown for only one curve per sub-plot for clarity. Inset in a) provides a close up for Q2 and Q3 events in water.

major contributor to the turbulent mass transfer. The same order of importance $\overline{u'_z c'}_{Q4} > \overline{u'_z c'}_{Q1} > \overline{u'_z c'}_{Q2} > \overline{u'_z c'}_{Q3}$ can be observed at all depth for the 10 ppm DPS run. There, all quadrant sorted turbulent mass fluxes decrease with decreasing z, both inside and outside of δ_v except at very small depths (top two depths of measurement). The difference between renewal and injection events does not seem to depend on depth z. For both water and DPS, turbulent events opposed to the mass transfer direction are not negligible, but the overall turbulence tends to promote mass transfer. Injection events are the main contributor to mass transfer in the two fluids. The mechanisms of turbulent mass transfer are yet quite different: in water, turbulence mostly acts close to the interface and less outside of the viscous sub-layer, while in DPS, the renewal and injection actions is spread over the full depth of the ROI, well outside the viscous sub-layer δ_v. Turbulent mass fluxes are quite intense in the bulk, reach a minimum at z/$\delta_v \simeq 0.27$ before further increasing.

4.4. Modelling of turbulent mass fluxes

A first approach modelling of turbulent mass flux at the interface is typically achieved by first order eddy-diffusivity or gradient models. The eddy diffusivity can be derived from the turbulent mass flux and expected concen-

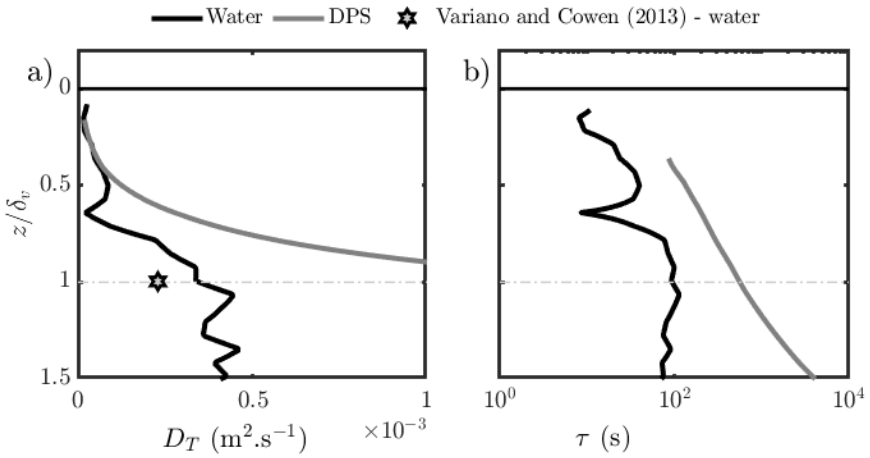

Figure 11: Profiles of D_T (a) and τ as a function of z/δ_v for water and DPS. The star in a) is the value reported in [2] for $z \simeq \delta_v$.

tration profile by using a gradient diffusion analogy [2, 45, 46]:

$$\overline{u'_z c'} \simeq -D_T \times \frac{\partial C}{\partial z} \tag{2}$$

Profiles for D_T for water and DPS are shown in figure 11 a). $D_T$increases with depth, as previously observed in water for $z > \delta_v$ by [2]. The value of D_T reported in the latter study for water at $z = \delta_v$ (star symbol in figure 11 a)) is in good agreement with the present data. In DPS, the increasing trend is much more pronounced and D_T values, which were close to that of water for $z \ll \delta_v$, increase by an order of magnitude when $z/\delta_v \to 1$. Non constant values broadly suggest that the Eddy-diffusivity model is not the best suited to describe near surface mass transfer from a modelling perspective conversely to case of classical boundary layers. A more elaborate mean gradient models described in [45, 46] is thus applied, in which the vertical turbulent mass flux is written as

$$\overline{u'_z c'} \simeq \tau \overline{u'_z}^2 \times \frac{\partial C}{\partial z} \tag{3}$$

with τ a model parameter homogeneous to a diffusion time. Profiles of τ are shown in figure 11 b). The value of τ also increases with depth, in a more pronounced fashion for DPS as compared to water. Indeed, in DPS, the expected concentration profiles quickly tend to asymptotic values and zero

gradients when moving outwards the viscous sub-layer (figure 3 e), while strong injection events and thus non negligible turbulent mass fluxes are still observed (figure 10), thus leading to larger τ values. This last figure illustrate the need to account for strong intermittent injection events in the modelling of mass transfer in DPS. Moreover, the way turbulence approaches the surface has to be questioned in regards to the different hypothesis necessary to obtain equation 3 from complete scalar transport equations. In particular, the nature of large eddies responsible for large instantaneous mass fluxes events may be significantly different here as compared to a classical boundary layer. In the case of classical boundary layers for which a mean flow, parallel to the surface exists, large scale events are intrinsically aligned in the flow direction, along the surface. In the present case, large structures are related to bulk turbulence properties and possibly grid oscillation making them more likely vertically oriented (perpendicular to the interface) in the bulk, and only constrained in their orientation and shape in the surface influenced layer, in which the dynamics is known to be affected by the presence of polymers [19]. In case of water the last modelling (equation 3, figure 11 b) could be acceptable if defining two distinct zones, inside δ_v and outside δ_v. For DPS however, the difference between such zones doesn't exists questioning the very use of δ_v, such as defined here, as a relevant boundary layer for modelling near-surface mass transfer. Future experiments performed on a larger ROI could allow to investigate deeper asymptotic behaviours and possibly define a more suitable characteristic depth for turbulent mass fluxes in non-Newtonian media.

5. Conclusion

In this work, turbulent dissolution and mass transfer of carbon dioxide into water and a moderately shear-thinning liquid phase was studied experimentally coupling SPIV and $I_{pH}^{(r)} - PLIF$. In both water and low concentration DPS, scalar fields in the sub-surface ROI consist in a complex combination of injection and renewal events. In the first 1 or 2 mm underneath the interface, a statistical concentration boundary layer establishes and takes the form of a long horizontal saturated patch, randomly broken or made thinner by renewal events. Below this scalar boundary layer, injection-type structures prevail. At the highest depths of the ROI, these patches are eventually broken and mixed. The presence of polymer promotes horizontal or vertical elongation of scalar structures, inside or outside the viscous sub-layer respec-

tively. Conditional analysis confirms that all four types of events relevant to vertical turbulent mass transfer (as defined by the quadrant decomposition) have non negligible probability of occurrence at all depths. Events in favour of downward mass fluxes (Q2 and Q4) are yet always respectively stronger, and mass transfer is effectively enhanced.

The physical mechanisms behind turbulent mass transfer are thus broadly similar in water and DPS: negative concentration fluctuation events have moderate c' amplitude but high probability, while positive concentration fluctuation occur at a larger range of c' but with lower probability. Renewal events are the most probable but only weakly contributing to mass transfer, while injection events are less probable but associated to higher concentration fluctuations and thus the major contributors to vertical turbulent mass transfer. The major difference between water and DPS, lays in the signature of those mechanisms, *i.e* the distribution of mass transfer events along depth. In water, most of the mass transfer events are concentrated inside the hydrodynamic viscous sub-layer, whereas in DPS, strong turbulent mass fluxes are observed at depth higher than δ_v, and a minimum value is found inside the viscous sub-layer.

Local measurement of turbulent mass fluxes such as those reported here are highly desirable in the context of mass transfer modelling, for which first order gradient model appear insufficient. Extensive effort has been and is still being made to relate mass transfer velocity k_L to local turbulence properties [20, 48] and our experimental contribution can be used to power this modelling effort, that is now facing the challenge of complex fluid rheology encountered in many industrial applications [49]. Three-component information brought by SPIV, or other more elaborate three-dimensional methods such as PTV [38] applied near-surface, could be useful in the context of surface divergence modelling [50, 48]. As for experiments, a natural next step further would be to investigate more shear-thinning fluids (higher polymer concentration) [25, 19] for which the hydrodynamic behaviour in the viscous sub-layer significantly differs from the Newtonian one. Classical boundary layer modelling tested here seems to fail, and this failure is even more remarkable with DPS, raising questions on the hypothesis at the origin of those models and the choice of the relevant length scales. Further study on the effect of the largest scales which are at the origin of the turbulence generation seems to be needed, both in water and DPS.

Acknowlegements

The authors thank Dr. Ing. H. Herlina, Prof. Gilles Hébrard and Prof. Alain Liné for the enriching discussions, and Prof. Stavroula Balabani for hosting and funding while this article was being written.

Conflicts of interest

The authors declare no conflicts of interest.

References

[1] J. G. Janzen, H. Herlina, G. H. Jirka, H. E. Schulz, J. S. Gulliver, Estimation of mass transfer velocity based on measured turbulence parameters, AIChE Journal 56 (8) (2010) 2005–2017.

[2] E. A. Variano, E. A. Cowen, Turbulent transport of a high-Schmidt-number scalar near an air–water interface, Journal of Fluid Mechanics 731 (2013) 259–287.

[3] T. Lacassagne, M. EL Hajem, F. Morge, S. Simoens, J.-Y. Champagne, Study of Gas Liquid Mass Transfer in a Grid Stirred Tank, Oil & Gas Science and Technology – Revue d'IFP Energies nouvelles 72 (1) (2017) 7.

[4] J. C. R. Hunt, Turbulence Structure and Turbulent Diffusion Near Gas-Liquid Interfaces, in: W. Brutsaert, G. H. Jirka (Eds.), Gas Transfer at Water Surfaces, no. 2 in Water Science and Technology Library, Springer Netherlands, 1984, pp. 67–82.

[5] B. H. Brumley, G. H. Jirka, Near-surface turbulence in a grid-stirred tank, Journal of Fluid Mechanics 183 (1987) 235–263.

[6] C. R. Chu, G. H. Jirka, Turbulent gas flux measurements below the air-water interface of a grid-stirred tank, International Journal of Heat and Mass Transfer 35 (8) (1992) 1957–1968.

[7] J. Magnaudet, I. Calmet, Turbulent mass transfer through a flat shear-free surface, Journal of Fluid Mechanics 553 (2006) 155–185.

[8] O. Flores, J. J. Riley, A. R. Horner-Devine, On the dynamics of turbulence near a free surface, Journal of Fluid Mechanics 821 (2017) 248–265.

[9] H. Herlina, J. G. Wissink, Isotropic-turbulence-induced mass transfer across a severely contaminated water surface, Journal of Fluid Mechanics 797 (2016) 665–682.

[10] J. G. Wissink, H. Herlina, Y. Akar, M. Uhlmann, Effect of surface contamination on interfacial mass transfer rate, Journal of Fluid Mechanics 830 (2017) 5–34.

[11] J.-C. Gabelle, F. Augier, A. Carvalho, R. Rousset, J. Morchain, Effect of tank size on kLa and mixing time in aerated stirred reactors with non-newtonian fluids, The Canadian Journal of Chemical Engineering 89 (5) (2011) 1139–1153.

[12] Y. Kawase, N. Hashiguchi, Gas—liquid mass transfer in external-loop airlift columns with newtonian and non-newtonian fluids, The Chemical Engineering Journal and the Biochemical Engineering Journal 62 (1) (1996) 35–42.

[13] A. A. Olajire, CO2 capture and separation technologies for end-of-pipe applications – A review, Energy 35 (6) (2010) 2610–2628.

[14] H. E. Huppert, J. A. Neufeld, The Fluid Mechanics of Carbon Dioxide Sequestration, Annual Review of Fluid Mechanics 46 (1) (2014) 255–272.

[15] N. Seyed Hosseini, H. Shang, J. A. Scott, Biosequestration of industrial off-gas CO2 for enhanced lipid productivity in open microalgae cultivation systems, Renewable and Sustainable Energy Reviews 92 (2018) 458–469.

[16] L. Li, H. S. Lim, Y. T. Kang, Mass transfer characteristics for CO2 absorption in nanoabsorbents, International Journal of Heat and Mass Transfer 129 (2019) 650–659.

[17] W. Henry, Experiments on the Quantity of Gases Absorbed by Water, at Different Temperatures, and under Different Pressures, Philosophical Transactions of the Royal Society of London 93 (1803) 29–276.

[18] W. K. Lewis, W. G. Whitman, Principles of Gas Absorption., Industrial & Engineering Chemistry 16 (12) (1924) 1215–1220.

[19] T. Lacassagne, S. Simoëns, M. EL Hajem, J.-Y. Champagne, Oscillating grid generating turbulence near gas-liquid interfaces in shear-thinning dilute polymer solutions, Physical Review Fluids 5 (3) (2020) 033301, publisher: American Physical Society.

[20] R. Higbie, The rate of absorption of a pure gas into still liquid during short periods of exposure,, New York, 1935.

[21] P. V. Danckwerts, Significance of Liquid-Film Coefficients in Gas Absorption, Industrial & Engineering Chemistry 43 (6) (1951) 1460–1467.

[22] H. Herlina, G. H. Jirka, Experiments on gas transfer at the air–water interface induced by oscillating grid turbulence, Journal of Fluid Mechanics 594 (2008) 183–208.

[23] W. E. Asher, H. Liang, C. J. Zappa, M. R. Loewen, M. A. Mukto, T. M. Litchendorf, A. T. Jessup, Statistics of surface divergence and their relation to air-water gas transfer velocity, Journal of Geophysical Research: Oceans 117 (C5) (2012) C05035.

[24] J. C. R. Hunt, J. M. R. Graham, Free-stream turbulence near plane boundaries, Journal of Fluid Mechanics 84 (02) (1978) 209–235.

[25] T. Lacassagne, S. Simoëns, M. EL Hajem, A. Lyon, J.-Y. Champagne, Oscillating grid turbulence in shear-thinning polymer solutions, Physics of Fluids 31 (8) (2019) 083102.

[26] J. Bodart, J.-B. Cazalbou, L. Joly, Direct numerical simulation of unsheared turbulence diffusing towards a free-slip or no-slip surface, Journal of Turbulence 11 (2010) N48.

[27] J. Magnaudet, High-Reynolds-number turbulence in a shear-free boundary layer: revisiting the Hunt-Graham theory, Journal of Fluid Mechanics 484 (2003) 167–196.

[28] V. R. Ranade, J. J. Ulbrecht, Influence of polymer additives on the gas-liquid mass transfer in stirred tanks, AIChE Journal 24 (5) (1978) 796–803.

[29] M. S. Puthli, V. K. Rathod, A. B. Pandit, Gas–liquid mass transfer studies with triple impeller system on a laboratory scale bioreactor, Biochemical Engineering Journal 23 (1) (2005) 25–30.

[30] F. Cabaret, L. Fradette, P. A. Tanguy, Gas–liquid mass transfer in unbaffled dual-impeller mixers, Chemical Engineering Science 63 (6) (2008) 1636–1647.

[31] Y. Kawase, A. De, Turbulent heat and mass transfer in newtonian and dilute polymer solutions flowing through rough pipes, International Journal of Heat and Mass Transfer 27 (1) (1984) 140–142.

[32] M. Han, G. González, M. Vauhkonen, A. Laari, T. Koiranen, Local gas distribution and mass transfer characteristics in an annulus-rising airlift reactor with non-Newtonian fluid, Chemical Engineering Journal 308 (2017) 929–939.

[33] A. B. Rodd, D. E. Dunstan, D. V. Boger, Characterisation of xanthan gum solutions using dynamic light scattering and rheology, Carbohydrate Polymers 42 (2) (2000) 159–174.

[34] F. Garcia-Ochoa, V. E. Santos, J. A. Casas, E. Gomez, Xanthan gum: production, recovery, and properties, Biotechnology Advances 18 (7) (2000) 549–579.

[35] N. B. Wyatt, M. W. Liberatore, Rheology and viscosity scaling of the polyelectrolyte xanthan gum, Journal of Applied Polymer Science 114 (6) (2009) 4076–4084.

[36] M. Lohse, E. Alper, G. Quicker, W.-D. Deckwer, Diffusivity and solubility of carbondioxide in diluted polymer solutions, AIChE Journal 27 (4) (1981) 626–631.

[37] T. Lacassagne, A. Lyon, S. Simoëns, M. E. Hajem, J.-Y. Champagne, Flow around an oscillating grid in water and shear-thinning polymer solution at low Reynolds number, Experiments in Fluids 61 (1) (2019) 15.

[38] T. Lacassagne, J. Vatteville, C. Degouet, M. El Hajem, S. Simoëns, PTV measurements of oscillating grid turbulence in water and polymer solutions, Experiments in Fluids 61 (7) (2020) 165.

[39] T. Lacassagne, S. Simoëns, M. EL Hajem, J.-Y. Champagne, POD analysis of oscillating grid turbulence in water and shear thinning polymer solution, AIChE Journal 67 (1) (2020) e17044.

[40] P. Valiorgue, N. Souzy, M. EL Hajem, H. Ben Hadid, S. Simoëns, Concentration measurement in the wake of a free rising bubble using planar laser-induced fluorescence (PLIF) with a calibration taking into account fluorescence extinction variations, Experiments in Fluids 54 (4) (2013) 1–10.

[41] T. Lacassagne, S. Simoëns, M. E. Hajem, J.-Y. Champagne, Ratiometric, single-dye, pH-sensitive inhibited laser-induced fluorescence for the characterization of mixing and mass transfer, Experiments in Fluids 59 (1) (2018) 21.

[42] T. Lacassagne, Oscillating grid turbulence and its influence on gas liquid mass transfer and mixing in non-Newtonian media, PhD Thesis, University of Lyon, INSA Lyon (2018).

[43] A. Vreme, F. Nadal, B. Pouligny, P. Jeandet, G. Liger-Belair, P. Meunier, Gravitational instability due to the dissolution of carbon dioxide in a Hele-Shaw cell, Physical Review Fluids 1 (6) (2016) 064301.

[44] J. M. Wallace, H. Eckelmann, R. S. Brodkey, The wall region in turbulent shear flow, Journal of Fluid Mechanics 54 (1) (1972) 39–48.

[45] J.-Y. Vinçont, S. Simoëns, M. Ayrault, J. M. Wallace, Passive scalar dispersion in a turbulent boundary layer from a line source at the wall and downstream of an obstacle, Journal of Fluid Mechanics 424 (2000) 127–167.

[46] S. Simoëns, J. Wallace, The flow across a street canyon of variable width - part 2: Scalar dispersion from a street level line source, Atmos. Environ. 42 (2008) 2489–2503.

[47] J. M. Wallace, Quadrant Analysis in Turbulence Research: History and Evolution, Annual Review of Fluid Mechanics 48 (1) (2016) 131–158.

[48] D. E. Turney, S. Banerjee, Air–water gas transfer and near-surface motions, Journal of Fluid Mechanics 733 (2013) 588–624.

[49] R. Petříček, T. Moucha, F. J. Rejl, L. Valenz, J. Haidl, Volumetric mass transfer coefficient in the fermenter agitated by Rushton turbines of various diameters in viscous batch, International Journal of Heat and Mass Transfer 115 (2017) 856–866.

[50] S. P. McKenna, W. R. McGillis, The role of free-surface turbulence and surfactants in air–water gas transfer, International Journal of Heat and Mass Transfer 47 (3) (2004) 539–553.

Appendix A. $I_{pH}^{(r)} - PLIF$ calibrations

The $R = f(pH)$ and $I^* = f(pH)$ for $I_{pH}^{(r)} - PLIF$ (DPS) and $I_{pH} - PLIF$ (water) are shown in figure A.12. I^* is the single color fluoresced light intensity normalized by its maximum value at pH=7. The processing steps on a given instantaneous fluoresced light signal for the $I_{pH}^{(r)} - PLIF$ method are illustrated in figure A.13. The intensity from color 1 (a) and color 2 (b) are used to compute the ratio R (c), which is then converted into ratio using the calibration curve from fig A.12. The pH (d) is then used to estimate the dissolved gas concentration (e,f) by numerical solving of dissolved carbon dioxide acid-base equilibria (see [42]).

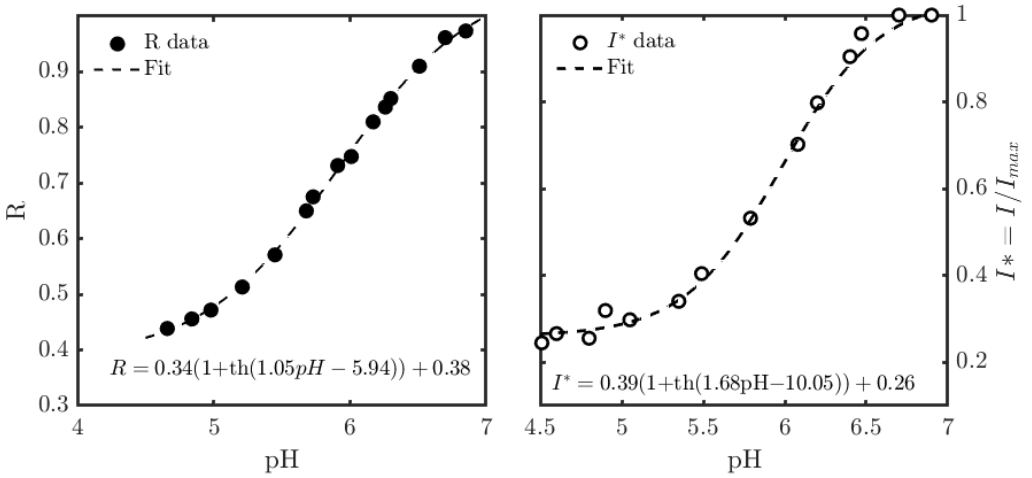

Figure A.12: Calibration curves for $R = f(pH)$ (left) and $I^* = f(pH)$ (right)

When a single color method is used, a "shortcut" from a single color intensity to the pH value is taken, as illustrated by the arrow on figure A.13, using the single color calibration curve from figure A.12.

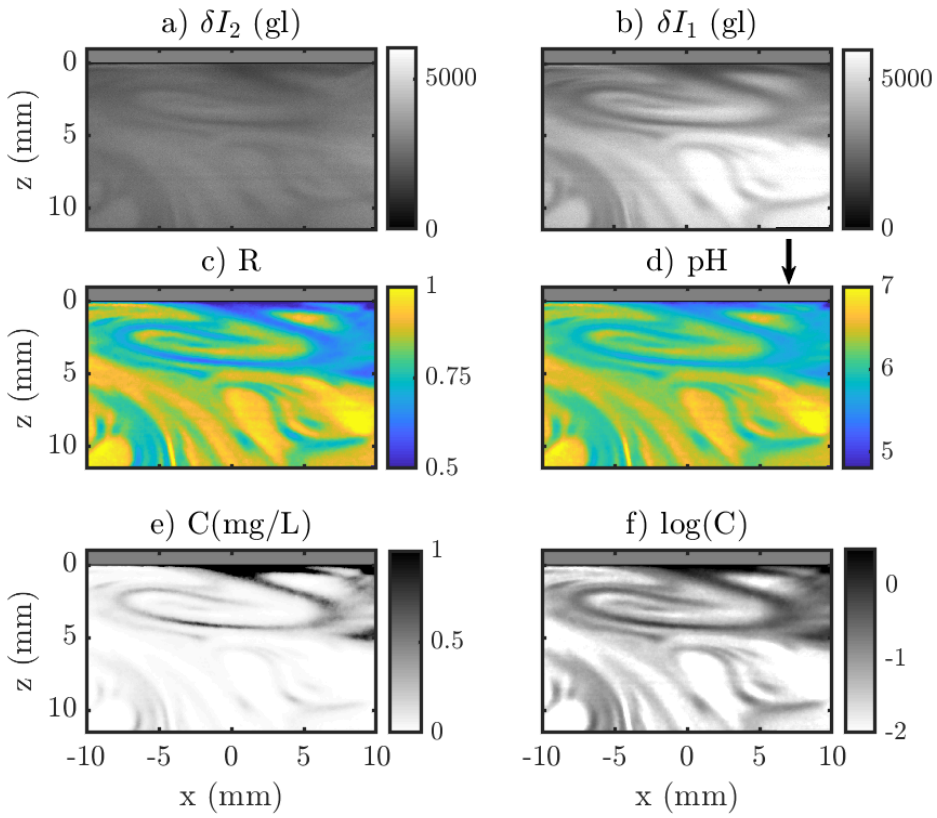

Figure A.13: Processing step of the $I_{pH}^{(r)} - PLIF$ method from the two color intensities (a,b) in gray level (gl) to Ratio (c), pH (d) and concentration fields in linear scale (e) and log scale (f).